APS physics

CHORUS

This is the accepted manuscript made available via CHORUS. The article has been published as:

Distinct behavior of localized and delocalized carriers in anatase TiO_{2} (001) during reaction with O_{2}

Chiara Bigi, Zhenkun Tang, Gian Marco Pierantozzi, Pasquale Orgiani, Pranab Kumar Das, Jun Fujii, Ivana Vobornik, Tommaso Pincelli, Alessandro Troglia, Tien-Lin Lee, Regina Ciancio, Goran Drazic, Alberto Verdini, Anna Regoutz, Phil D. C. King, Deepnarayan Biswas, Giorgio Rossi, Giancarlo Panaccione, and Annabella Selloni

Phys. Rev. Materials **4**, 025801 — Published 28 February 2020

DOI: 10.1103/PhysRevMaterials.4.025801

Distinct behaviour of localised and delocalised carriers in anatase TiO_2 (001) during reaction with O_2

Chiara Bigi,[1,2] Zhenkun Tang,[3,4] Gian Marco Pierantozzi,[1] Pasquale Orgiani,[1,5] Pranab Kumar Das,[1,6] Jun Fujii,[1] Ivana Vobornik,[1] Tommaso Pincelli,[1] Alessandro Troglia,[1,2] Tien-Lin Lee,[7] Regina Ciancio,[1] Goran Drazic,[8] Alberto Verdini,[1] Anna Regoutz,[9] Phil D. C. King,[10] Deepnarayan Biswas,[10] Giorgio Rossi,[1,2] Giancarlo Panaccione,[1,*] and Annabella Selloni[3,†]

[1] *Istituto Officina dei Materiali (IOM)-CNR, Laboratorio TASC, in Area Science Park, S.S.14, Km 163.5, I-34149 Trieste, Italy.*
[2] *Dipartimento di Fisica, University of Milano, Via Celoria 16, I-20133 Milano Italy.*
[3] *Department of Chemistry, Princeton University, Princeton, New Jersey 08544, USA.*
[4] *Department of Physics, Hengyang Normal University, 16 Heng-Hua Road, Zhu-Hui District, Hengyang, 421008, P. R. China.*
[5] *CNR-SPIN, UOS Salerno, Via Giovanni Paolo II 132, 84084 Fisciano, Italy.*
[6] *International Centre for Theoretical Physics (ICTP), I-34100 Trieste, Italy.*
[7] *Diamond Light Source, Harwell Science and Innovation Campus, Didcot OX11 0DE, United Kingdom.*
[8] *Department for Materials Chemistry, National Institute of Chemistry, Hajdrihova 19, SI- 1001 Ljubljana, Slovenia.*
[9] *Department of Materials, Imperial College London, South Kensington, London SW7 2AZ, United Kingdom.*
[10] *SUPA, School of Physics and Astronomy, University of St. Andrews, St. Andrews KY16 9SS, United Kingdom.*

Two-dimensional (2D) metallic states induced by oxygen vacancies (V_Os) at oxide surfaces and interfaces provide opportunities for the development of advanced applications, but the ability to control the behavior of these states is still limited. We used Angle Resolved Photoelectron Spectroscopy (ARPES) combined with Density Functional Theory (DFT) to study the reactivity of V_O-induced states at the (001) surface of anatase TiO_2, where both 2D metallic and deeper lying in-gap states (IGs) are observed. The 2D and IG states exhibit remarkably different evolution when the surface is exposed to molecular O_2: while IGs are almost completely quenched, the metallic states are only weakly affected. DFT calculations indeed show that the IGs originate from surface V_Os and remain localized at the surface, where they can promptly react with O_2. In contrast, the metallic states originate from subsurface vacancies whose migration to the surface for recombination with O_2 is kinetically hindered on anatase TiO_2 (001), thus making them much less sensitive to oxygen dosing.

I. INTRODUCTION

Many functional properties of anatase TiO_2 of relevance, e.g., in photocatalysis, solar cells and sensors are critically affected by the presence of excess electrons induced by intrinsic defects, dopants or photoexcitation[1–7]. Understanding and controlling the behaviour of excess electrons is thus essential for improving TiO_2's performance in existing applications and for developing new applications as well. In particular, the chemical doping arising from oxygen vacancies (V_Os) induces important changes in the electronic structure, such as the creation of in-gap defect states, the formation of depletion regions, and band bending[3,8]. Another noteworthy feature connected with V_Os is the presence, under photoirradiation, of electronic states with metallic d-character (Ti 3d) at the anatase (101) and (001) surfaces, generally termed two-dimensional electron gas (2DEG) states[9–13]. First observed at the $LaAlO_3/SrTiO_3$ (LAO/STO) interface[14], 2DEGs have been reported both in transition metal oxides (TMOs) parent compounds (e.g. bare surfaces of $SrTiO_3$ and $KTaO_3$) and in engineered heterostructures[15,16]. Nevertheless, a number of important aspects are not yet settled, such as the depth distribution of the oxygen vacancies acting as electron donors. Another critical issue is the behaviour of 2DEG and localised in-gap (IG) defect states under reducing vs. oxidising conditions, notably to what extent and in what conditions it is possible to control the excess of V_Os created by photoirradiation[9,10,17].

Here we combine ultraviolet (UV) and X-ray based electron spectroscopies and first principles DFT calculations to clarify the role, the formation mechanism and the possible control of defect states formed at the (001) surface of anatase TiO_2[18–20]. In-situ UHV growth of high quality epitaxial thin films obtained by Pulsed Laser Deposition (PLD) allowed us to identify the types of defect states that either appear under photoirradiation or can be induced and tailored by means of controlled post-growth treatment (UHV annealing). ARPES measurements confirm the existence of both localised and delocalised electronic states, while Resonant-PES in the soft X-ray range identifies their character as Ti^{3+} and Ti^{4+}, respectively. Spectral changes were monitored while molecular O_2 was steadily fluxed on the sample surface through a metallic capillary[21–23]. Remarkably, the results reveal that 2DEG delocalized features are robust against oxygen exposure, whilst the localised IG states are suppressed. Comparison with DFT calculations provides evidence of a distinct depth-dependence of defect states. The 2DEG originates from subsurface V_Os and resides in sub-surface layers due to the attractive potential resulting from these V_Os. In contrast, the deeper lying IG states that are suppressed by O_2 originate from the surface V_Os. Our results also pro-

* giancarlo.panaccione@elettra.eu
† aselloni@princeton.edu

vide a consistent explanation of previous contrasting findings and suggest possible strategies for controlling the carriers concentration and transport at the surface of anatase.

II. EXPERIMENTAL AND COMPUTATIONAL METHODS

II.1. Growth

Anatase TiO_2 thin films were grown by Pulsed Laser Deposition (PLD) at a dedicated chamber located at the APE-IOM laboratory (NFFA facility, Trieste, Italy)[24]. Rutile TiO_2 single-crystal was ablated using a KrF excimer pulsed laser source kept at about 2 J/cm2 energy density, with a typical laser repetition rate of 3 Hz. The substrate was kept at 700°C growth temperature, while oxygen background pressure was set to 10^{-4} mbar. Annealed samples have been kept at the growth temperature for 10 minutes in UHV (PLD chamber base pressure is the range of 10^{-7} mbar). Anatase TiO_2 thin films were grown on (001)-oriented $LaAlO_3$ (LAO) substrates. Epitaxial strain-less condition was verified for these films. All the samples presented in this work are $\sim$ 20 nm thick.

II.2. Transmission and Scanning Transmission Electron Microscopy

Cs probe-corrected Jeol ARM 200 CF scanning transmission electron microscope with cold-FEG electron source, operated at 200 kV was used for high-resolution imaging of the samples. Electron Energy Loss Spectroscopy (EELS) was performed using Gatan dual-EELS Quantum ER system and elemental chemical analyses were performed with Centurio Jeol Energy Dispersive X-ray Spectroscopy (EDXS) system with 100 mm^2 SDD detector. Cross-sectional samples in the [010] zone axis suitable for TEM/STEM analyses have been obtained by a conventional polishing technique followed by dimpling and ion milling.

II.3. Ultraviolet ARPES, Soft X-ray ARPES, RESPES

The as-grown samples were directly transferred in-situ to the Angle-Resolved Photoemission (ARPES) end-station installed on the Low-Energy branch of APE beamline (APE-LE) at Elettra synchrotron (Trieste, Italy). Such a chamber is equipped with a Scienta DA30 hemispherical electron energy and momentum analyser (30° angular acceptance), which allows to map the electronic bands over the extended areas of the Brillouin zone without rotating the sample. ARPES experiments were performed at a base pressure $\sim 10^{-10}$ mbar and with the samples kept at liquid Nitrogen. Photon energy of 46 eV was used with the light incidence angle of 45°. All the light polarisation available at the beamline have been exploited (linear vertical, linear horizontal, circular right and circular left). When not otherwise specified, the overall energy resolution was set to $\sim$40 meV, and the angular resolution was set to 0.2° (corresponding to $\sim$ 0.01 $Å^{-1}$ at 46 eV photon energy).

Soft x-ray ARPES, Resonant Photoemission (RESPES) and oxygen dosing were performed at I09 beamline at Diamond light source (Didcot, UK). The samples fabricated at the APE-IOM laboratory were transferred to the Soft X-Ray branch of I09 beamline 120 by means of a UHV suitcase. The surface's contamination was thus prevented throughout the whole experiment. Sample temperature was 90 K. In order to reduce the effects of higher order components coming from the beamline optics in the resonant photoemission measurements, the monochromator has been tuned to obtain the best compromise between flux, resolution and higher order rejection. Furthermore, the residual second-order contribution was subtracted in all spectra. The energy position of the Fermi energy (E_F) and the energy resolution have been estimated by measuring the Fermi edge of poly-Au foil in thermal and electric contacts with the sample. The overall energy resolution (analyser + beamline) was kept below 250 meV for the entire photon energy range. Molecular oxygen was injected through a metallic capillary placed close to the sample surface (i.e. $\sim 1-2$ cm). The amount of oxygen has been monitored by means of a Residual Gas Analyser (RGA) available in the experimental chamber. Base pressure in the experimental chamber was $1{\cdot}10^{-10}$ mbar, up to a maximum O_2 partial pressure of $4{\cdot}10^{-9}$ mbar.

II.4. Computational Details

DFT calculations for pristine and reduced anatase (001) were performed using the Vienna Ab Initio Simulation Package (VASP)[25,26]. We used the projector augmented-wave (PAW) pseudopotentials to describe the electron-ion interactions and the PBE functional[27] within the generalized gradient approximation (GGA) to treat the exchange-correlation interaction between electrons. The energy cut-off for the expansion of the wave-functions was set to 500 eV. Since GGA is affected by the self-interaction error that favours delocalized electronic states, selected calculations using the PBE+U method with U = 3.9 eV[28] were also carried out in order to check the robustness of the PBE solutions (note that U values in the range 2.5-4 eV are typically used to describe defect states in TiO_2[29,30]). While predicting a more structured electronic charge distribution in comparison to pure PBE, these PBE+U calculations confirmed the delocalized character of the subsurface excess electron states at the anatase (001) surface[31], which was reported also in a previous PBE+U study[32].

We modeled the anatase TiO_2 (001)-(1×4) surface using a repeated slab geometry. We considered slabs of 8 TiO_2 layers with a (3×4) surface supercell for calculations of defect formation energies, in order to minimize interactions between defects in periodic replicas, and slabs of 12 TiO_2 layers with a (2×4) surface su-

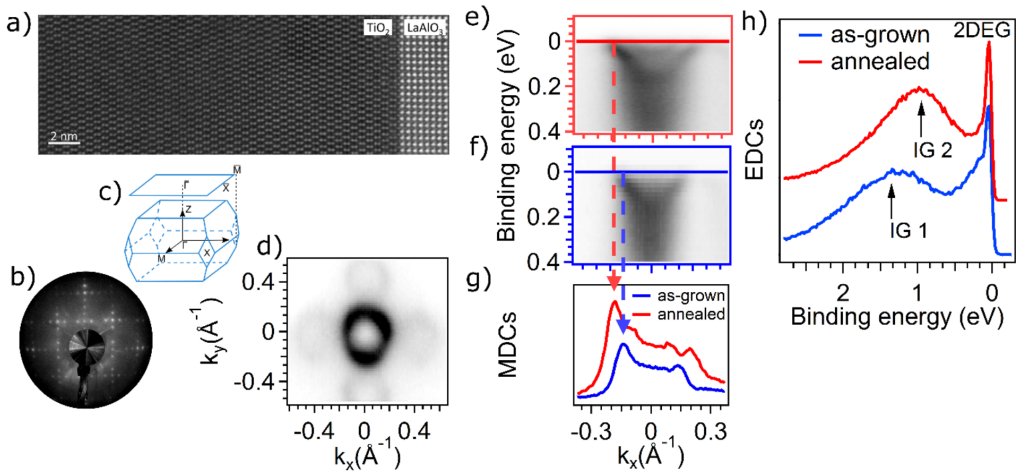

FIG. 1. (a) Representative high-resolution Z-contrast image of the TiO_2/LAO interfacial region. (b) LEED pattern ($\sim$ 110 eV) showing the $(1\times4)-(4\times1)$ surface reconstruction of the anatase thin films. (c) Sketch of the first BZ of anatase. (d) Fermi surface contour, measured at 46 eV photon energy, covering the first BZ, obtained by superimposing the Fermi surfaces measured with different light polarisations. (e), (f) ARPES spectra of the metallic state acquired at hν=46 eV photon energy around the $\overline{\Gamma}$ point of the second Brillouin zone ($\overline{\Gamma}_1$): (e) 2DEG of anatase film with high amount of oxygen vacancies after the annealing treatment; (f) 2DEG of as-grown film. (g) MDCs at the Fermi level, in correspondence of the straight lines in panels (e) and (f)) for the annealed (red) and as-grown (blue) samples respectively; the dashed lines highlight the position of the Fermi momenta k_F. (h) EDCs extracted at the k_F of the outer band for the annealed (red) and the as-grown (blue) samples.

percell for calculations of the electronic structure and charge densities. The vacuum region between consecutive slabs was larger than 12 Å and dipole corrections were added to remove the electric field in this region[33]. A $3\times2\times1$ Monkhorst-Pack mesh was used to sample the Brillouin zone (BZ). All atoms of the slab were relaxed except those in the two bottom layers, which were kept fixed at their bulk positions. Geometry optimizations were carried out with convergence thresholds of 10^{-4} eV and 10^{-2} eV/Å for the total energy and the forces on the ions, respectively. Reaction pathways were determined using the climbing image nudged elastic band method[34].

Oxygen vacancies were created by removing a neutral oxygen atom. The resulting neutral V_Os consist of a vacant site, effectively bearing a 2+ positive charge, and two compensating excess electrons. Their formation energies were calculated as $E_{form}(V_O) = E_{def} - E_{stoich} + 1/2E_{tot}(O_2)$, where E_{def} and E_{stoich} are the total energies of the reduced (defective) and stoichiometric (defect-free) slabs, respectively, and $E_{tot}(O_2)$ is the total energy of the O_2 molecule.

III. EXPERIMENTAL RESULTS

III.1. Structural and Ultraviolet ARPES results

Epitaxial strainless anatase TiO_2 thin films were grown by PLD on LAO substrates. Details of the growth protocol and structural characterization by X-ray diffraction are given elsewhere[24]. The results of our cross-sectional high-resolution Transmission Electron Microscopy (TEM) and high-angle annular dark-field scanning TEM (HAADF-STEM) measurements are shown in Fig. 1. In panel a), a representative high-resolution Z-contrast image shows an atomically sharp interface region. The typical dumbbell structure of Ti ions in TiO_2 anatase is clearly distinguishable in the film and occurs in the entire film region with no sign of presence of secondary phases. The crystal quality of the films extends up to the surface, as confirmed by the Low Energy Electron Diffraction (LEED) $(1\times4)-(4\times1)$ surface reconstruction pattern in panel b)[9,10,24].

ARPES measurements were performed along the $\overline{\Gamma}$-$\overline{X}$ direction of the surface projected Brillouin zone (Fig. 1c), obtained by superimposing the Fermi surfaces measured with different light polarisations (i.e. linear horizontal and vertical, circular right and left). With such a procedure we could compensate the lack of intensity due to symmetry-related selection rules typically occurring for bands of d_{xy} orbital character. The surface structural reconstruction is reflected in the Fermi surface measured in the first Brillouin zone, shown in Fig. 1d and the Supplemental Material[31]: The bright circle centred at the $\overline{\Gamma}$ point corresponds to a 2DEG, characterised by a parabolic dispersion (Fig. 1e and 1f) and a d_{xy} orbital character arising from Ti 3d states typical in TMOs[9,11,15,35]. In addition, several replicas occur along both k_x and k_y directions, arising from the periodic lateral perturbation induced by the surface $(1\times4)-(4\times1)$ reconstruction[11,20]. Panels e) and f) compare the E vs. k dispersion of the 2DEG for UHV annealed and as-grown samples respectively. Both the as-grown and reduced samples were transferred in-situ in UHV (i.e. without exposure to air) for the ARPES experiments. Two dispersive parabolic-like states are evident in Fig. 1e: an outer parabola and a second (faint) quantized sub-band related to the confinement potential at the surface[11,12]. The bottom of the two quan-

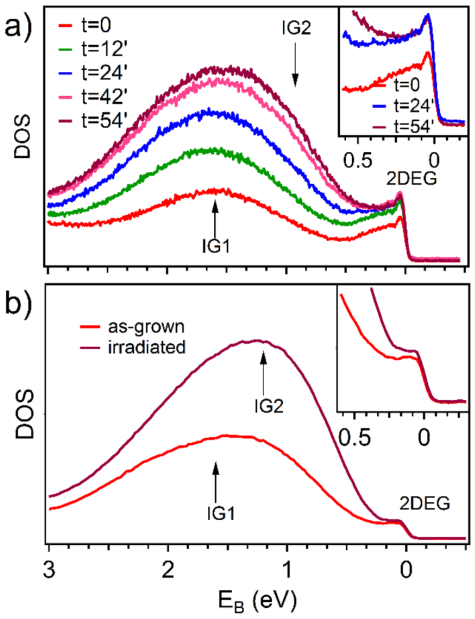

FIG. 2. DOS of anatase films deposited on LAO and measured at (a) APE beamline (Elettra; hv=46 eV) in the highest beam flux condition available and (b) I09 beamline (Diamond Light Source; hv=120 eV); in both panels, arrows indicate the position of the IGs for the as-grown and annealed samples, as discussed in the main text.

tized states is located at $\sim$ 180 meV and $\sim$ 65 meV for the outer and the inner band respectively, while the Fermi momenta (k_F) are at $\sim$ 0.18 Å^{-1} and $\sim$ 0.11 Å^{-1}. These values are 25% larger than those obtained for the as-grown sample reported in Fig. 1f. In addition, the bands of the annealed sample are located at $\sim$ 45 meV higher binding energies. All these changes confirm electron doping of the sample due to the increase of V_Os by annealing, as observed elsewhere[30].

For a direct comparison between the Fermi wavevectors k_F of the annealed and as-grown samples, Fig. 1g reports the momentum distribution curves (MDCs) at the Fermi energy E_F for the two films (red/blue lines in panel e/f respectively), while Fig. 1h shows the Energy Distribution Curves (EDCs) obtained from panel e and f at the two different k_F vectors. In the latter, a broad intense non-dispersive state is found between $\sim$ 1eV and 2 eV of binding energy (BE), corresponding to localized IG states[13,22]. In the annealed samples, the spectral weight of IG states is shifted towards the Fermi energy; the asymmetric shape of the peak is consistent with the presence of a second in-gap state at lower BE ($\sim$1 eV). Such state appears also upon beam irradiation and its spectroscopic intensity reaches a saturation value (see below). A further significant spectral change in the two EDCs of Fig. 1h is present at the Fermi energy: a shoulder on the 2DEG peak of the as-grown sample weakens after the annealing, consistently with an increased number of free carriers in the sample[9–12]. The electron carrier density values for the two samples are $n_{2D}^{as-grown} = 3{\cdot}10^{13}$ and $n_{2D}^{annealed} = 5{\cdot}10^{13}$ cm^{-2}, as calculated for two dimensional states with spin-degenerate bands[36].

The effects of intense beam irradiation on the electronic properties of oxide surfaces, including TiO_2, have been investigated extensively[10,13,22,37,38]. Fig. 2a reports the evolution of the spectral intensity vs. time. The DOS of the pristine surface (red curve, t=0) displays IG states at $\sim$1.6 eV BE. Under beam irradiation, the intensity of the DOS in the in-gap region increases and stabilises after roughly 1 hour of beam exposure. Similar to the IG states, the metallic 2DEG intensity also increases and saturates after about 25-30 minutes of beam irradiation. These findings agree with previous results[10,13], and are consistent with the evolution vs. time observed at the Diamond Light Source. The asymmetric shape of the peak in both curves of Fig. 2b indicates the presence of at least a second, distinct, in-gap state. Similar to changes observed upon annealing, photo-irradiation favours the formation of an IG located at shallower binding energies (i.e. $\sim$1 eV BE). This may indicate that the localised states are related to two inequivalent oxygen vacancy sites and that the formation of the latter is more favourable under the beam.

III.2. Soft-X ray ARPES, Resonant Photoemission (RESPES) and dosing experiment

While some reports suggest that the metallic state has a 3D character[9] a model linking the metallic state to the specific anatase surface arrangement has recently been shown to provide excellent agreement with the experimental data[11]. The 2D nature of the metallic state is also supported by experiments studying both the effect of electron doping through alkaline adsorption and the influence of beam irradiation at the anatase surface[10,12]. To gain further insight, we have performed soft X-ray ARPES and Resonant PES (RESPES) experiments, while simultaneously compensating the production of oxygen vacancies arising from photoirradiation. This has been achieved during the measurements by *in-operando* fluxing molecular oxygen through a metal capillary positioned in the proximity of the sample surface[21–23]. Fig. 3 shows the ARPES spectra acquired in the second BZ for the pristine sample in UHV (i.e. base pressure $1{\cdot}10^{-10}$ mbar) measured with linearly polarised radiation of hν = 120 eV (panel a) and ARPES measured on the very same sample while dosing the surface with oxygen (i.e. base pressure $4{\cdot}10^{-9}$ mbar; partial O_2 pressure $4{\cdot}10^{-10}$ mbar) (panel b). In Fig. 3c, the MDCs extracted at E_F from panels a) and b) are compared.

The value of k_F is reduced from 0.19 Å^{-1} to 0.15 Å^{-1} ($\sim$20%) under oxygen dosing, i.e. it shows the opposite trend compared to that observed upon annealing in Fig. 1e and 1f, giving direct evidence of (partial) healing of V_Os and consequent reduction of the number of free electron carriers at the surface, in agreement with previous reports[9]. Such a decrease corresponds to a reduction in the carrier density of $\sim$60%, qualitatively consistent with the theoretical picture for subsurface vacancies presented below. Fig. 3d compares the angle-integrated Density of States (DOS) extracted from panels 3a and 3b with a BE range covering also the IG states. Almost com-

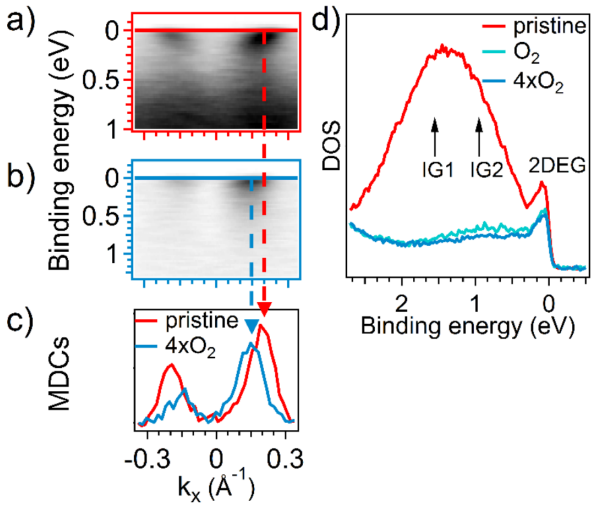

FIG. 3. ARPES spectra of a pristine as-grown (a) sample and (b) with molecular O_2 dosing ; (c) MDCs extracted at E_F (red and light blue straight lines in panels (a) and (b) respectively indicate where the MDCs have been extracted); (d) Evolution of the DOS upon oxygen dosing (red line corresponds to partial pressure P = $1{\cdot}10^{-10}$ mbar, light blue P = $1{\cdot}10^{-9}$ mbar and dark blue P = $4{\cdot}10^{-10}$ mbar).

plete suppression of the IG states is observed as soon as oxygen is dosed; the residual IG intensity is little affected by further increase of the oxygen partial pressure (4 times the initial value), dropping below the background signal (it is visible only at resonance, see next section). Conversely, the 2DEG spectral weight is only slightly decreased and the reduction is mainly ascribable to the changes in the background signal. We also stress that the 2DEG maximum healing was already achieved at the lower oxygen partial pressure, as an increment of the oxygen pressure up to four times the initial dose (i.e. from 10^{-9} mbar to $4{\cdot}10^{-9}$ mbar recorded on RGA) did not further affect the 2DEG state. Such a distinct behaviour of IG and 2DEG has not been reported before in anatase TiO_2.

In contrast to our results, studies on $SrTiO_3$ have shown that both the IG and the 2DEG are completely suppressed under O_2 dosing, with the spectral weights of the two states reducing at the same pace[15,17,22,38–40]. While incomplete compensation of the 2DEG was observed at the buried interface between a 4 u.c. epitaxial $LaAlO_3$ deposited on $SrTiO_3$[22], in our study we are not sensitive to the film-substrate interface due to the short probing depth typical of photoemission spectroscopies. Therefore, our results should be compared to the bare $SrTiO_3$ rather than the LAO/STO buried interface.

The different reactivities of the IG and 2DEG in anatase suggest that these states may arise from different oxygen vacancy sites inside the material. Moreover, since the O_2 exposure in our setup occurs at the surface, the healing of the oxygen defects strongly depends on the V_O capability to migrate inside the material. The suppression of the IG suggests that the relative oxygen vacancies are located either at the surface or at buried sites that can easily move to the surface and recombine with the adsorbed molecules, as observed in anatase (101)[41]. Conversely, the 2DEG insensitivity against O_2 dosing indicates that the migration of the corresponding vacancies to the surface is unlikely, at least in the examined pressure and temperature range.

The electronic character of the 2DEG and the localized IG states was investigated by means of resonant photoemission (RESPES) measurements at the Ti $L_{2,3}$ edges. As both IG and 2DEG arise from Ti 3d states[11,12], RESPES provides additional information by exploiting the energy shift between the core levels of titanium atoms with different oxidation states. Fig. 4a shows the X-ray absorption spectra (XAS) measured in TEY across the Ti L_3 edge from an as-grown sample (red curve) and under oxygen dosing (dark blue curve).

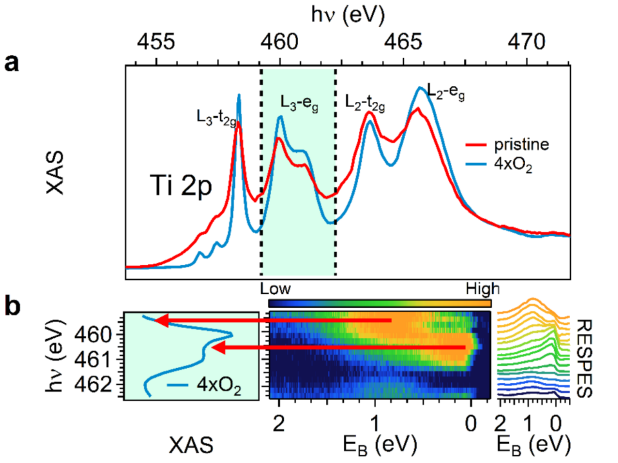

FIG. 4. (a) XAS spectra at Ti $L_{2,3}$ of a pristine (red) and during oxygen dosing (blue); (b) ResPES in the second BZ of upon oxygen dosing (colour map - central panel - displays the momentum-integrated photoemission intensity; the resonant DOS curves show the different resonating energies for the IG and the 2DEG states(red arrows) are reported on the right.

The four main peaks (located at approximate excitation energies of 458.3 eV, 460.5 eV, 463.5 eV, and 465.5 eV excitation energies) can be ascribed to the combination of spin-orbit splitting of the initial states (L_3-L_2) and crystal field splitting of the d orbitals in the final state (t_{2g}-e_g) for Ti atoms in 4+ oxidation state. The additional splitting of the L_3-e_g peak ($\sim$ 460.5 eV) is the fingerprint of the anatase phase arising from distortion of the ideal octahedron around Ti atom and long-range effects[42–44].

Effects of O_2 dosing on the absorption spectrum (total yield) edges of anatase TiO_2 film were measured at 90 K. Pristine sample refers to base pressure in the chamber of $1{\cdot}10^{-10}$ mbar, while the dark blue curve corresponds to the highest oxygen partial pressure of the present work ($4{\cdot}10^{-9}$ mbar). Upon oxygen dosing, the spectral intensity is lowered in the pre-edge as well as in the valleys at $\sim$459 eV and $\sim$462.5 eV, which correspond to spectral lines of Ti^{3+}[43]. As found in similar systems, e.g. rutile TiO_2[45] and $SrTiO_3$[46], the observed changes can be directly linked to the number

of oxygen vacancies.

ResPES in the second BZ were acquired upon oxygen dosing (P = $1{\cdot}10^{-9}$ mbar). The angle integrated photoemission EDCs, displayed as a color map in Fig. 4b, indicate that the IG and 2DEG states resonate at different photon energies. The IG is peaked at an energy corresponding to a Ti^{3+} oxidations state, i.e. the valley at ∼459.3 eV (roughly 0.8 eV away from the resonance of the 2DEG states), in agreement with previous results[22,24]. Conversely, the 2DEG follows the same trend of the XAS, with maximum intensity located around the L_3-e_g doublet at ∼460.5 eV (characteristic of the stoichiometric Ti^{4+}). Similarly, above 462 eV (i.e. in the valley before the L_2-edge) the IG intensity rises first.

To better decouple the IGs and the 2DEG signals, we further investigated the DOS evolution at E_F as a function of the photon energy before and during oxygen dosing (Fig. 5a and 5b). The IG states are strongly suppressed with oxygen dosing, yet both their BE and their resonating behavior are not affected. The signal of the 2DEG is much clearer in panel b), due to the strong suppression of the IG intensity upon oxygen dosing. Resonant angle-resolved-photoemission (ResARPES) spectra, acquired in the 2BZ across the Ti L_3-e_g absorption edge while dosing oxygen at the surface, are shown in Fig. 5c. The IG state is well visible as non-dispersive red broad line which resonates at the lowest photon energy (i.e. at 458.5 eV), whereas the electron pocket at Fermi is localized in the BZ centre, more intense in the middle of the photon energy scan (459.7 eV). Figs. 5d and 5e show the intensities of the IG and 2DEG states across the Ti L_3-e_g absorption edge. Each square (dot) in panel 5d (panel 5e) corresponds to ARPES spectra acquired at different photon energy. The coloured rectangles in the top-left panel of Fig. 5c mark the binding energy/momentum region where the spectral intensity has been integrated. For both states two regions of momentum space were selected: the projected 2BZ centre ($\overline{\Gamma}_1$) and a low symmetry momentum region. For the IG state, these correspond to the black and grey rectangles, respectively. Similarly, the spectral intensity at the Fermi level has been integrated in the same momentum ranges (i.e. centre of 2BZ (orange) and outside (brown)). The intensity of the IG state shows the same trend in both k regions, as expected for a localized state, while the 2DEG state disperses having zero intensity outside the centre (i.e. beyond 0.2 $Å^{-1}$ from $\overline{\Gamma}_1$). In both panels 5d and 5e the total electron yield acquired during the measurement is showed for comparison. As in the case of the angle integrated spectra, it appears that the 2DEG state resonates with the L_3-e_g doublet, whereas the in-gap state has Ti character, as it resonates on the rising edge of the L_3-t_{2g} peak, out of the Ti^{4+} resonance.

Altogether, these findings provide evidence that: i) the 2DEG and the IG states could be related to distinct V_O sites and the former is robust against oxygen dosing ii) the IGs are strongly localised on Ti atoms close to vacancy sites (Ti^{3+}) while the 2DEG wavefunction is delocalised over many Ti sites that largely maintain the Ti^{4+} oxidation state found in pristine TiO_2.

III.3. THEORETICAL RESULTS

The observed different dependence of IG and 2DEG states to oxygen dosing suggests that they could be linked to different vacancy sites. To confirm this hypothesis, we performed DFT calculations of surface and subsurface V_Os at the anatase (001)-(1 × 4) surface, with the underlying assumption that photoirradiation creates oxygen vacancies at the top few layers and vacancy diffusion to the bulk is negligible at the low temperature of our experiment[38]. We described the reconstructed surface using the widely accepted model of Ref.[20], where ridges exposing twofold coordinated oxygen (O_{2c}) and four-fold Ti atoms (Ti_{4c}) are separated by terraces exposing O_{2c}, three-fold O (O_{3c}) and five-fold Ti (Ti_{5c}) atoms with a (1 × 4) periodicity (Fig.6a). We used slabs of 8 TiO_2 layers with a (3 × 4) surface supercell to calculate V_O formation energies at the different surface and subsurface sites shown in Fig.6a.

From the computed V_O formation energies (Fig.6b), it appears that oxygen vacancies are most likely to occur at surface VO1 (ridge O_{2c}) and VO4 (terrace O_{3c}) sites as well as at subsurface VO6 and VO7 sites, while the surface VO2 and VO3 sites are energetically unfavourable. From the charge density plots in Fig.6d-i and the Supplemental Material[31], it also appears that the character of the defect states is very different for surface and subsurface V_Os, as these states become increasingly less localized moving from the surface to the subsurface. In particular, the two excess electrons from the vacancy are well localized on the Ti atoms adjacent to the vacant site and form deep energy levels in the band gap in the case of VO1, in agreement with previous calculations by Shi et al.[47]. In contrast, the defect states are partially delocalized in the case of VO4 and VO5 and become fully delocalized over few (001) planes in the case of subsurface VO6 and VO7 (and deeper V_Os as well), where they give rise to shallow energy levels at the bottom of the conduction band[31]. The delocalized character of subsurface defect states is confirmed by PBE+U calculations with U=3.9 eV, reported in the Supplemental Material[31].

The electrostatic potential profile in the surface region was computed from the energies of the semi-core Ti 3s levels in different layers of the slab in the absence/presence of V_Os[31]. As shown in Fig.6c, the potential becomes repulsive near the surface of a defect-free slab[11,32], and this effect is further enhanced in the presence of VO1 (green line). In contrast, VO4 (blue) and VO7 (red) induce an attractive potential well of depth ∼ 0.2 eV (very similar for VO4 and VO7) that confines the excess electron states in the subsurface Ti layers. Note that, unlike in previous modelling studies[11], this confining potential emerges naturally in our calculations for the reduced slabs.

To model the effect of oxygen dosing, we considered the adsorption of an O_2 molecule on the anatase surface with a surface or subsurface V_O (Fig. 7). O_2

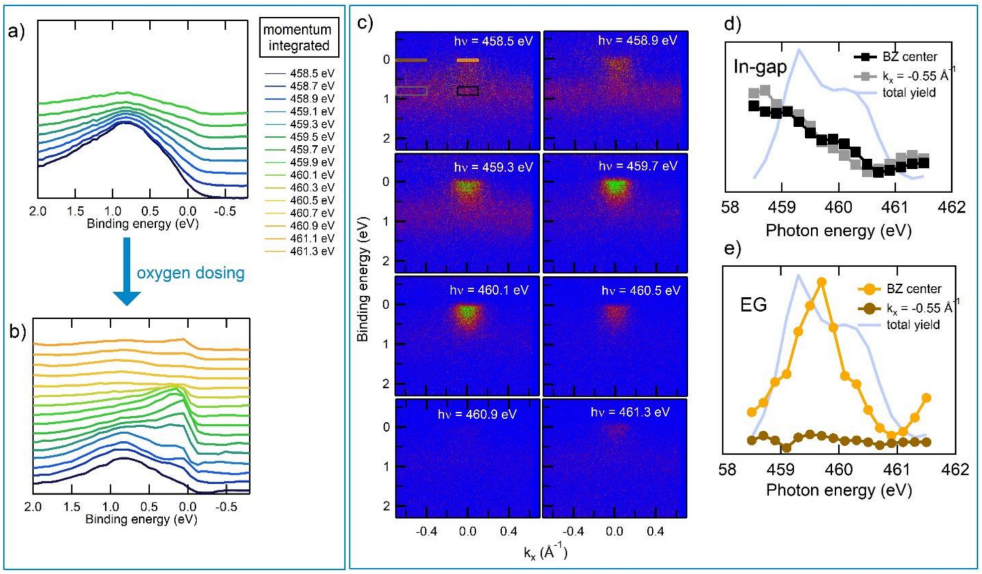

FIG. 5. (a), (b) DOS evolution at the Fermi level as a function of the photon energy before and during oxygen dosing; (c) Resonant angle-resolved-photoemission (ResARPES) spectra acquired while dosing oxygen; (d), (e) Intensity of the IG and 2DEG states across the Ti L_3-e_g absorption edge respectively.

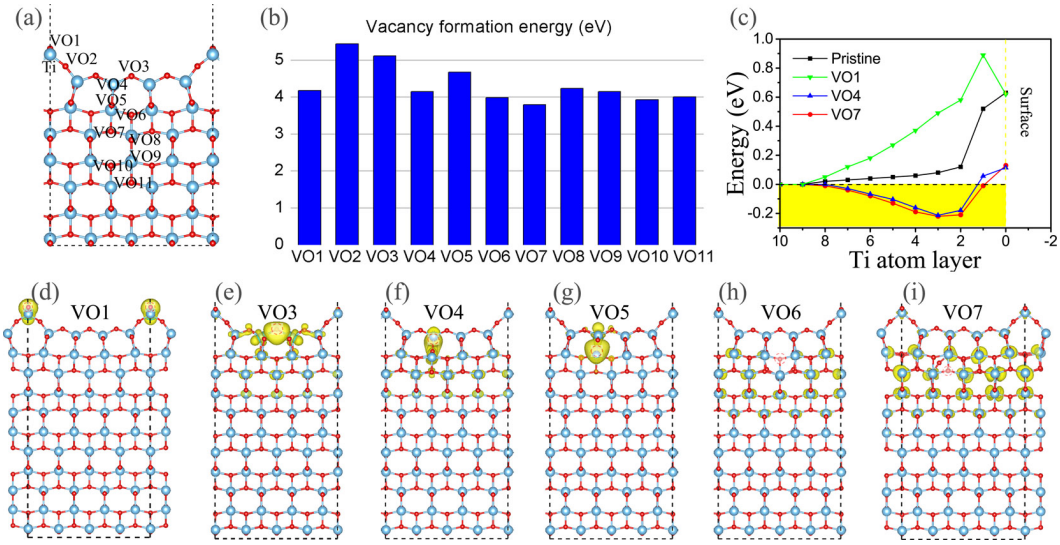

FIG. 6. (a) Side view of the reconstructed anatase TiO_2(001)-1 × 4 slab model; the investigated oxygen vacancy sites are indicated; Ti and O atoms are light blue and red, respectively. (b) V_O formation energies (eV; blue bars) at different surface and subsurface oxygen sites computed using DFT-PBE; (c) Electrostatic potential profile in the surface region, computed from the shift of the Ti 3s peak in the different Ti layers of the pristine and reduced slabs with VO1, VO4 or VO7 defects. Here, layer 0 corresponds to the ridge Ti_{4c} sites, layer 1 to the terrace Ti_{5c} sites, and so forth. The yellow shading highlights the region of negative (attractive) potential; (d,e,f,g,h,i) Charge density contours of the excess electron states induced by VO1, VO3, VO4, VO5, VO6 and VO7, respectively; the vacancy positions are indicated by dashed red circles; dashed black lines show the unit cell used for the calculations. Additional density contours are shown in Supplemental Material[31].

adsorption on TiO_2 is known to involve the transfer of excess electrons from the oxide to the molecule[1,3,41,48]. In the presence of a VO1, O_2 undergoes a strongly exothermic and barrier-less adsorption at the vacancy site[31], which results in the formation of a bridging peroxide (O_2^{2-}) at the ridge, denoted $(O_2)_o$ in Fig. 7. The two excess electrons of VO1 are both transferred to the adsorbed species, so that no excess electron remains in TiO_2, consistent with the strong reduction of the IG signal observed in ARPES when exposing the surface to O_2.

A different picture holds for the adsorption of O_2 on a surface with subsurface V_Os. In this case, O_2 adsorbs at a terrace Ti_{5c} site and only one of the two excess electrons of the vacancy transfers to the molecule[1,3,48], thus resulting in the formation of an adsorbed superoxide (O_2^-), denoted O_2* in Fig. 7. As previously discussed for the reaction of O_2 with the reduced anatase (101) surface[41], the negatively charged adsorbate has an attractive interaction with the subsurface vacancy, so that migration of V_O toward the surface would be energetically favourable (Fig. 7a). At variance with

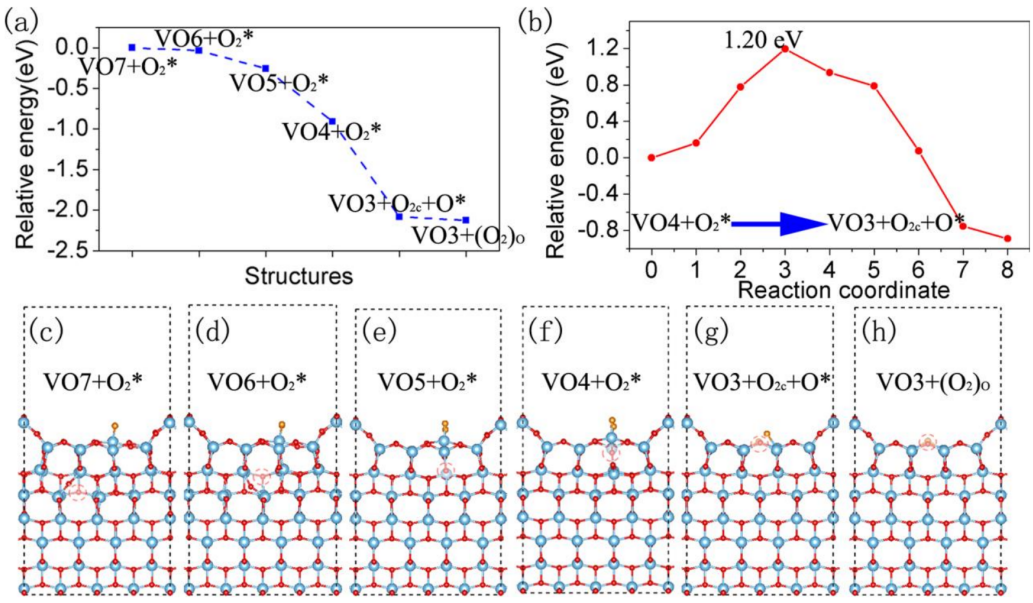

FIG. 7. (a) O_2 adsorption energy as a function of the subsurface (VO4 VO7) or surface (VO3) oxygen vacancy location. Relevant structures with a subsurface VO, denoted VOn+O_2* (n=4-7), are shown in panels (c-f). For VO3, two nearly degenerate structures are present, as shown in panels (g-h), where O* indicates an oxygen adatom and $(O_2)_O$ a bridging peroxide replacing an O_{2c}. The energy zero corresponds to the adsorption energy of VO7+O_2*. (b) Energy barrier for the diffusion of an O-vacancy from VO4 to VO3 in the presence of adsorbed oxygen. (c-h) Atomic geometries of adsorbed O_2 on reduced anatase (001) with a subsurface (VO4-VO7) or surface (VO3) oxygen vacancy, as described in (a). Ti atoms are blue, O atoms are red, adsorbed O_2 is orange; dashed red circles indicate the positions of the vacant sites.

what found for anatase (101)[41], however, the energy barrier for subsurface → surface migration of the V_O is quite high at the anatase (001) surface[49], at least for the O_2 concentration considered here, as shown by Fig. 7b for the case of the VO4→ VO3 migration step. It is thus quite likely that the V_O remains subsurface at the low temperature of our experiment, so that the adsorbed O_2 remains a superoxide, i.e. one of the two excess electrons of the vacancy remains in TiO_2. This explains the persistence of the 2DEG at the anatase-TiO_2(001) as well as the decrease in the number of carriers observed under oxygen dosing without the necessity to include any interface effect with the substrate in the calculation.

IV. CONCLUSIONS

In summary, our results reveal distinct behaviours of localized and delocalized states induced by oxygen vacancies at the surface of anatase TiO_2. Due to their different spatial locations and the kinetics of defect diffusion in anatase, the 2D delocalized states are much more robust than the localised in-gap states when exposed to molecular oxygen in a wide range of pressures. This robustness of the delocalized states is an important feature that could be exploited for different applications, e.g. to tune the electronic structure of TiO_2 in engineered interfaces and heterostructures, or to precisely control the concentration of charge carriers in photo-sensitive devices.

Our findings unveil a new and relevant aspect of the surface chemistry of TiO_2, providing a pathway to tailor the performance of future devices.

ACKNOWLEDGMENTS

This work has been partly performed in the framework of the nanoscience foundry and fine analysis (NFFA-MIUR Italy) facility. We thank Fabio Miletto Granozio (Spin-CNR) and Ralph Claessen (Univ. Wurzburg) for useful discussions. A.S. acknowledges the support of DoE-BES, Division of Chemical Sciences, Geo sciences and Biosciences under Award DE-SC0007347. Z. T. was supported by the National Natural Science Foundation of China (No. 51602092), the Science and Technology Innovation Project Foundation of Hunan Province (No. 2018RS3103). GD acknowledges the financial support from Slovenian Research Agency (P2-0393). E. Cociancich from CNR-IOM and A. Di Cristoforo from Universita' Politecnica delle Marche are gratefully acknowledged for the support in the TEM specimen preparation.

AUTHOR CONTRIBUTIONS

G.P., C.B., P.O. and G.M.P. conceived the experiment(s), A.S. planned the computational studies. G.P., C.B., P.O., G.M.P. and A.S. wrote the paper with contributions from J.F, I.V., Z.T. All authors discussed the results, commented manuscript and prepared written contributions. P.O. grew the films, G.D and R.C. characterized samples. Z. T. performed the calculations. C.B., G.M.P., A.V., T.L.L., A. R., P.D.C.K., G.R., A.T., T.P., D.B., P.K.D., performed synchrotron radiation experiments and analysed the data. C.B. and G.M.P. contributed equally to this

work.

[1] T. L. Thompson, J. T. Yates, *Chemical Reviews* **106 (10)**, 4428-4453 (2006).
[2] A. Fujishima, X. Zhang, D. A. Tryk, Surface Science Reports **63 (12)**, 515-582 (2008).
[3] U. Diebold, Surface Science Reports **48 (5)**, 53-229 (2003).
[4] C. Di Valentin, G. Pacchioni, A. Selloni, Journal of Physical Chemistry C **113 (48)**, 20543-20552 (2009).
[5] M. A. Henderson, Surface Science Reports **66 (6-7)**, 185-297 (2001).
[6] S. X. Zhang, D. C. Kundaliya, W. Yu, S. Dhar, S. Y. Young, L.G. Salamanca-Riba, S. B. Ogale, R. D. Vispute, T. Venkatesan, Journal of Applied Physics **102 (1)**, 013701 (2007).
[7] J. Bai, B. Zhou, Chemical Reviews *114 (19)*, 10131-10176 (2014).
[8] A. G. Thomas, W. R. Flavell, A. K. Mallick, A. R. Kumarasinghe, D. Tsoutsou, N. Khan, C. Chatwin, S. Rayner, G. C. Smith, R. L. Stockbauer, S. Warren, T. K. Johal, S. Patel, D. Holland, A. Taleb, F. Wiame, Physical Review B **75 (3)**, 035105 (2007).
[9] S. Moser, L. Moreschini, J. Jacimovic, O. S. Barisic, H. Berger, A. Magrez, Y. J. Chang, K. S. Kim, A. Bostwick, E. Rotenberg, L. Forro', M. Grioni, Physical Review Letters **110 (19)**, 196403 (2013).
[10] T. C. Rodel, F. Fortuna, F. Bertran, M. Gabay, M. J. Rozenberg, A. F. Santander-Syro, P. Le Fevre, Physical Review B **92**, 041106(R) (2015).
[11] Z. Wang, Z. Zhong, S. McKeown Walker, Z. Ristic, J. Z. Ma, F. Y. Bruno, S. Ricco', G. Sangiovanni, G. Eres, N. C. Plumb, L. Patthey, M. Shi, J. Mesot, F. Baumberger, M. Radovic, Nano Letters **17 (4)**, 2561-2567 (2017).
[12] R. Yukawa, M. Minohara, D. Shiga, M. Kitamura, T. Mitsuhashi, M. Kobayashi, K. Horiba, H. Kumigashira, Physical Review B **97 (16)**, 165428 (2018).
[13] Y. Aiura, K. Ozawa, E. F. Schwier, K. Shimada, K. Mase, The Journal of Physical Chemistry C **122 (34)**, 19661-19669 (2018).
[14] A. Ohtomo, H. Y. Hwang, Nature **427**, 423 (2004).
[15] A. F. Santander-Syro, O. Copie, T. Kondo, F. Fortuna, S. Pailhes, R. Weht, X. G. Qiu, F. Bertran, A. Nicolaou, A. Taleb-Ibrahimi, P. Le Fevre, G. Herranz, M. Bibes, N. Reyren, Y. Apertet, P. Lecoeur, A. Barthelemy, M. J. Rozenberg, Nature **469**, 189 (2011).
[16] P. D. C. King, R. H. He, T. Eknapakul, P. Buaphet, S. K. Mo, Y. Kaneko, S. Harashima, Y. Hikita, M. S. Bahramy, C. Bell, Z.Hussain, Y. Tokura, Z. X.Shen, H. Y. Hwang, F. Baumberger, W. Meevasana, Physical Review Letters **108 (11)**, 117602 (2012).
[17] W. Meevasana, P.D.C King, R.H. He, S.K. Mo, M. Hashimoto, A. Tamai, P. Songsiriritthigul, F. Baumberger, Z.X. Shen, Nature materials **10 (2)**, 114-118, (2011).
[18] R. Hengerer, B. Bolliger, M. Erbudak, M. Gratzel, Surface Science **460 (1)**, 162-169 (2000).
[19] G. S. Herman, M. R. Sievers, Y. Gao, Physical Review Letters **84**, 3354 (2000).
[20] M. Lazzeri, A. Selloni, Physical Review Letters **87 (26)**, 266105 (2001).
[21] L. Dudy, M. Sing, P. Scheiderer, J. D. Denlinger, P. Schutz, J. Gabel, M. Buchwald, C. Schlueter, T.-L. Lee, R. Claessen, Advanced Materials **28 (34)**, 7443-7449 (2016).
[22] J. Gabel, M. Zapf, P. Scheiderer, P. Schutz, L. Dudy, M. Stbinger, C. Schlueter, T. L. Lee, M. Sing, R. Claessen, Physical Review B **95 (19)**, 195109 (2017).
[23] T.-L. Lee, D. A. Duncan, Synchrotron Radiation News, **31 (4)**, 16-22, (2018).
[24] B. Gobaut, P. Orgiani, A. Sambri, E. Di Gennaro, C. Aruta, F. Borgatti, V. Lollobrigida, D. Ceolin, J.-P. Rueff, R. Ciancio, C. Bigi, P.K. Das, J. Fujii, D. Krizmancic, P. Torelli, I. Vobornik, G. Rossi, F. Miletto Granozio, U. Scotti di Uccio, G. Panaccione, ACS Applied Materials and Interfaces **9 (27)**, 23099-23106 (2017).
[25] G. Kresse, J. Furthmuller, Physical Review B **54 (16)**, 11169-11186 (1996).
[26] G. Kresse, J. Furthmuller, Comput. Mater. Sci. **6 (1)**, 15 (1996).
[27] J. P. Perdew, K. Burke, M. Ernzerhof, Physical Review Letters *77 (18)*, 3865-3868 (1996).
[28] M. Setvin, C. Franchini, X. Hao, M. Schmid, A. Janotti, M. Kaltak, C. G. Van de Walle, G. Kresse, U. Diebold, Physical Review Letters **113 (8)**, 086402 (2014).
[29] Z. Hu, H. Metiu, The Journal of Physical Chemistry C **115 (13)**, 5841-5845 (2011).
[30] P. Scheiber, M. Fidler, O. Dulub, M. Schmid, U. Diebold, W. Hou, U. Aschauer, A. Selloni, Physical Review Letters **109 (13)**, 136103 (2012).
[31] See Supplemental Material at http://link.aps.org/supplemental/xxxxx for pictures of the Fermi surface as a function of light polarization, computed PBE band structure for pristine and reduced anatase (001)-(1 × 4), computed layer-resolved Ti-3*s* density of states, DFT+U calculations for reduced anatase, potential energy profile for the adsorption of an O_2 molecules at a VO1 site.
[32] S. Selcuk, A. Selloni, Nature Materials **15**, 1107 (2016).
[33] L. Bengtsson, Phys. Rev. B **59**, 12301 (1999).
[34] G. Henkelman, B. P. Uberuaga, H. Jonsson, The Journal of Chemical Physics**113 (22)**, 9901-9904 (2000).
[35] P. D. C. King, S. McKeown Walker, A. Tamai, A. de la Torre, T. Eknapakul, P. Buaphet, S. K. Mo, W. Meevasana, M. S. Bahramy,F. Baumberger, Nature Communications **5**, 3414 (2014).
[36] J. M. Luttinger, Physical Review **119 (4)**, 1153-1163 (1960).
[37] N. C. Plumb, M. Salluzzo, E. Razzoli, M. Mansson, M. Falub, J. Krempasky, C. E. Matt, J. Chang, M. Schulte, J. Braun, H. Ebert, J. Minar, B. Delley, K. J. Zhou, T. Schmitt, M. Shi, J. Mesot, L. Patthey, M. Radovi, Physical Review Letters 113 (8), 086801 (2014).
[38] S. M. Walker, F. Y. Bruno, Z. Wang, A. de la Torre, A. Ricco, A. Tamai, T. K. Kim, M. Hoesch, M. Shi, M. S. Bahramy, P. D. C. King, F. Baumberger, *Advanced Materials* **27 (26)**, 3894-3899 (2015).
[39] C. Mathieu, S. Gonzalez, C. Lubin, O. Copie, V. Feyer, C. M. Schneider, N. Barrett, Surface and Interface Analysis **51 (1)**, 7-11, (2019).
[40] V. N. Strocov, A. Chikina, M. Caputo, M.-A. Husanu, F. Bisti, D. Bracher, T. Schmitt, F. Miletto Granozio, C. A. F. Vaz, and F. Lechermann, Physical Review Materials, **3 (10)**, 106001, (2019).
[41] M. Setvin, U. Aschauer, P. Scheiber, Y.-F. Li, W. Hou, M. Schmid, A. Selloni, U. Diebold, Science **341 (6149)**, 988 (2013).
[42] P. Kruger, Physical Review B **81 (12)**, 125121 (2010).

[43] F. M. F. de Groot; M. O. Figueiredo, M. J. Basto, M. Abbate, H. Petersen, J. C. Fuggle, Physics and Chemistry of Minerals **19 (3)**, 140-147 (1992).
[44] S. O. Kucheyev, T. van Buuren, T. F. Baumann, J. H. Satcher, T. M. Willey, R. W. Meulenberg, T. E. Felter, J. F. Poco, S. A. Gammon, L. J. Terminello, Physical Review B **69 (24)**, 245102 (2004).
[45] P. Le Fevre, J. Danger, H. Magnan, D. Chandesris, J. Jupille, S. Bourgeois, M. A. Arrio, R. Gotter, A. Verdini, A. Morgante, Physical Review B **69 (15)**, 155421 (2004).
[46] C. Chen, J. Avila, E. Frantzeskakis, A. Levy, M. C. Asensio, Nature Communications **6**, 8585 (2015).
[47] Y. Shi, H. Sun, M. C. Nguyen, C. Wang, K. Ho, W. A. Saidi, J. Zhao, Nanoscale **9 (32)**, 11553-11565 (2017).
[48] Y.-F. Li, A. Selloni, Journal of the American Chemical Society **135 (24)**, 9195-9199 (2013).
[49] S. Selcuk, X. Zhao, A. Selloni, Nature Materials **17 (10)**, 923-928 (2018).